Lawrence Berkeley National Laboratory
LBL Publications

Title
Pressure transient analysis during CO2 push-pull tests into faults for EGS characterization

Permalink
https://escholarship.org/uc/item/4wt3124n

Authors
Jung, Yoojin
Doughty, Christine
Borgia, Andrea
et al.

Publication Date
2018-09-01

DOI
10.1016/j.geothermics.2018.05.004

Peer reviewed

Pressure transient analysis during CO_2 push-pull tests into faults for EGS characterization

Yoojin Jung[a] Christine Doughty[a] Andrea Borgia[ad] Kyung Jae Lee[ae] Curtis M. Oldenburg[a] Lehua Pan[a] Thomas M. Daley[a] Rui Zhang[b] Bilgin Altundas[c] Nikita Chugunov[c] T.S. Ramakrishnan[c]

Abstract

With the goal of detecting and characterizing faults and fractures in enhanced geothermal systems (EGS), a new technology involving CO_2 push-pull testing, active-source geophysical imaging, and well logging has recently been proposed. This technique takes advantage of (1) the contrasting properties of supercritical CO_2 and water which cause CO_2 to appear distinct from surrounding brine in seismic and other geophysical logging approaches, (2) the non-wetting nature of CO_2 which keeps it localized to the faults and fractures to create contrast potentially sufficient for active seismic and well-logging approaches to image faults and fracture zones at EGS sites. In this study, we evaluate the feasibility of using pressure transient monitoring during CO_2 push-pull tests to complement active seismic and wireline well logging for EGS characterization. For this purpose, we developed a 2D model of a prototypical geothermal site (Desert Peak, NV) that includes a single fault. The fault zone consists of a slip plane, fault gouge, and damage zone, and is bounded by the surrounding matrix of the country rock. Through numerical simulation using iTOUGH2, we found that the pressure transient at the monitoring wells in the fault gouge shows unique traits due to the multiphase flow conditions developed by CO_2 injection, and varies sensitively on the arrival of the CO_2 plume and the degree of CO_2 saturation. A sensitivity analysis shows the pressure transient is most sensitive to the fault gouge permeability, but also depends on multiphase flow parameters and the boundary conditions of the fault. An inversion study reveals that the fault gouge permeability can be best estimated with the pressure transient data, whereas additional CO_2 saturation data do not improve the accuracy of the inversion significantly.

Keywords: Enhanced geothermal sites (EGS), CO_2 push-pull, Pressure transient, Desert Peak geothermal field, Sensitivity analysis, Parameter estimation, Inverse modeling, iTOUGH2

1. Introduction

Enhanced geothermal systems (EGS) are engineered geothermal reservoirs that benefit from the ability to control fracturing and fracture flow. For successful EGS, it is essential to characterize faults and fracture networks(both natural and induced) at EGS sites. To achieve this goal, a new methodology has been proposed and evaluated, which uses CO_2 push-pull testing to enhance imaging of fractures and faults at EGS sites (Borgia et al., 2015, Borgia et al., 2017a, Borgia et al., 2017b; Oldenburg et al., 2016; Zhang et al., 2015). This technique involves (1) injection and withdrawal of CO_2into/out of fault/fracture zone, (2) imaging the induced contrast with active seismic and well logging approaches, and (3) characterizing the fault/fracture zone with the complementary data provided by (1) and (2). Natural and induced faults and fractures at EGS sites are difficult to characterize using traditional seismic or well-logging imaging techniques because faults/fractures filled with ambient brine are indistinguishable from surrounding matrix at EGS conditions. Supercritical CO_2 injected for the push-pull well testing helps increase seismic contrast because of the high compressibility of CO_2, which significantly reduces the stiffness tensor and consequently seismic velocity, electrical contrast because of the low electrical conductivity of CO_2 compared to brine, and neutron capture contrast because of the displacement of water. The additional benefit of using CO_2 is that CO_2 has a strong tendency to flow in faults and fractures due to its non-wetting characteristics. CO_2 replaces the formation brine in fault/fractures and effectively increases the contrast in geophysical properties between fault/fractures and matrix while tending to resist dispersing into the matrix. The enhanced contrast in seismic and well logging arising from CO_2 saturation can be used to detect and characterize the fault/fracture zone.
In this study, we evaluated the pressure transient analysis during CO_2 push-pull to complement active seismic and wireline well logging for EGS characterization. Pressure transient testing is one of the essential tools to

explore and monitor subsurface formations, and is used to infer geometric and flow properties as well as multiphase flow conditions. For this study, we developed a discretized model domain with a single dipping fault based on a highly simplified conceptual model of the Desert Peak geothermal field (Borgia et al., 2017a, Borgia et al., 2017b). We used TOUGH2/ECO2N V2.0 (Pruess et al., 2012; Pan et al., 2016) to simulate pressure transients during the injection (push period) and withdrawal (pull period) of CO_2 into the fault zone. We present here the characteristics of these pressure transients and examine the feasibility and effectiveness of pressure transient data interpretation for EGS characterization.

2. Geologic setting – Desert Peak geothermal field

The Desert Peak geothermal field is located in the northern Hot Springs Mountains ~80 km east-northeast of Reno, Nevada, and is within the northwest Great Basin, which is known as one of the most geothermally active regions in the USA. The Desert Peak geothermal field is largely controlled by NNE-striking, WNW-dipping normal faults (Faulds et al., 2004), and the geothermal field is on the left side of a set of parallel, closely spaced faults in these fault systems. This set of faults is linked by multiple subvertical faults of high fracture density, which are favorable for upward flow of hydrothermal fluids (Faulds et al., 2010). The reservoir temperature is measured at 207–218 °C (Faulds et al., 2010; Shevenell and De Rocher, 2005).

Fig. 1 shows the geologic map of the Deseart Peak geothermal field (modified from Faulds et al., 2012) and the cross section projecting through the central part of the Rhyolite Ridge fault zone. The geothermal field is largely composed of Miocene volcanic and sedimentary rocks that overlie a Mesozoic basement, and the range is dissected by the NNE-striking normal faults. The 2D model domain we consider is marked with a red rectangular box in the cross-section view. Details of structural and geologic features of the Desert Peak geotheraml field can be found in Faulds et al. (2010).
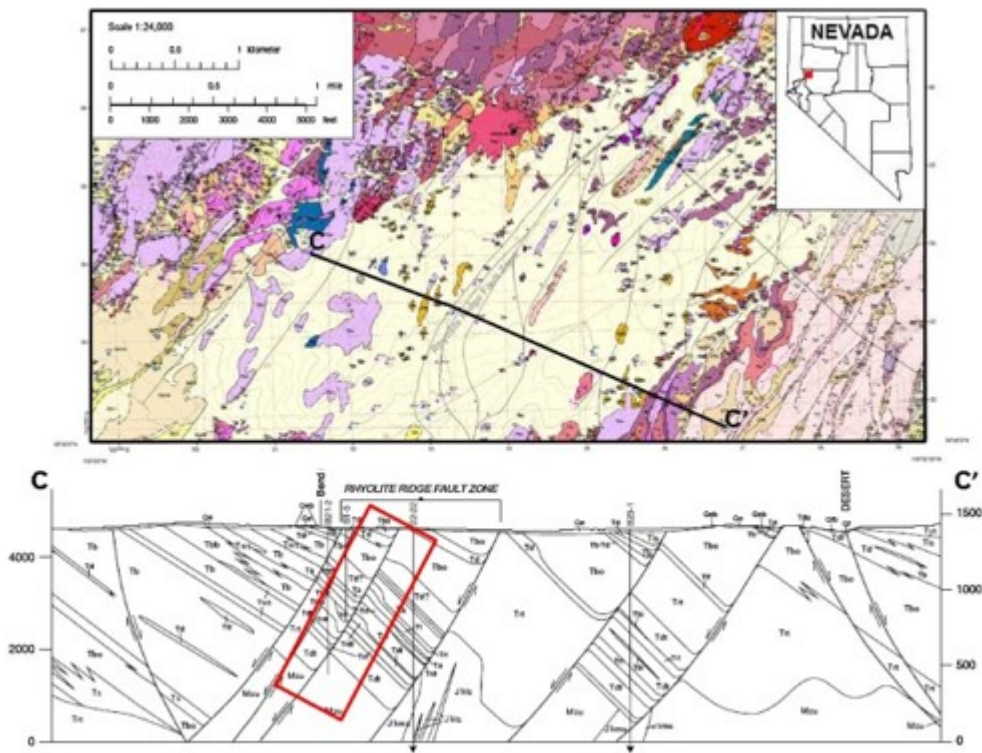
Fig. 1. Geologic map of the Deseart Peak geothermal field (modified from Faulds et al., 2012) and cross section CC'. The cross section cuts the NNE-striking Rhyolite Ridge normal fault zone. In ascending order, unit abbreviations cut by the subvertical fault of interest (red retangular box in the cross section): Mzu, Mesozoic basement; Tdt, Trt, Oligocene ash-flow tuffs; Trdl, Oligo-Miocene rhyolite-dacite lavas; Trl, Oligo-Miocene rhyolite lavas; Tt, late Oligocene-early Miocene tuff; Ta, early to middle Miocene andesite-dacite lavas; Ttf, middle Miocene ash-flow tuff; Tbo, older basalt lavas; Td, diatomite. See Faulds et al. (2012) for description of other geologic units.

3. Model setup and parameters

3.1. Model development

We used TOUGH2/ECO2N V2.0 (Pruess et al., 2012; Pan et al., 2016) to develop a model and simulate the two-phase flow of CO_2 and water during CO_2 push-pull injection-withdrawal. This code is able to simulate two-phase flow in the pressure and temperature range up to 600 bar and 300 °C, respectively, and is therefore appropriate for EGS applications. Here, consistent with the terminology in TOUGH2/ECO2N, a CO_2-rich non-wetting phase is referred to as a gas phase. iTOUGH2-PEST (Finsterle, 1993; Finsterle, 2004; Finsterle et al., 2016; Finsterle and Zhang, 2011) is used for sensitivity and inverse analysis.

We developed a simplified 2D model including a single fault based on the geologic features of the Desert Peak geothermal field. We adapted and expanded the model domain originally developed by Borgia et al., 2017a, Borgia et al., 2017b to explore the technical feasibility of CO_2 push-pull testing for EGS fault/fracture characterization for pressure transient analysis. Similar to the conceptual model of a fault zone from Gudmundsson et al. (2002), the fault zone in our model consists of a slip plane, fault gouge, and damage zone, and it is bounded by the surrounding country rock. The fault gouge is formed during fault slip, and this crushed rock primarily consists of breccia and other clay-size particles. The gouge may include one or multiple thin slip planes, which are characterized by finer particles, polished surfaces and striations. In general, slip planes and fault gouges have higher permeabilities than the other rock types. The damage zone refers to the fractured rock developed at the outer boundary of the fault gouge during fault −slip events and extends into the unfaulted country rock. The fault gouge, damage zone, and country rock matrix have distinct fluid-flow properties (i.e., permeability and porosity), and such differences are taken into account in our model (see Table 1). In our 2D model, the fault gouge is 5 m thick on both sides of the slip plane (10 m total), and the damage zone is 10 m thick on both sides of the fault gouge. The matrix is 200 m thick on both sides of the damage zone, which is sufficiently wide to minimize the effect of the side boundaries. The model takes into account the variable country rocks for the matrix, as color-coded in Fig. 2. Table 1 shows the hydrological properties of each structure in the model.

Table 1. Hydrological and multiphase flow parameters.

Hydrogeologic property	Permeability [m²]	Porosity	Rock grain density [kg/m³]	Relative permeability parameters	Capillary pressure parameters
Slip plane		0.3		van Genuchten (1980)[a] $\lambda_{relp} = 0.8$; $S_{lr} = 0.23$; $S_{grmax} = 0.0$; $k_{rgmax} = 0.5$; $\gamma = 0.5$; $\lambda_{gas} = 0.9$	van Genuchten[b] $\lambda_{pcap} = 0.444$; $S_{lr} = 0.23$; $P_0 = 5.0 \times 10^2$ [Pa]; $P_{max} = 1.0 \times 10^8$[Pa]; $S_{lmin} = 0.03$
Fault gouge	$k_x = 10^{-12}$ $k_z = 2 \times 10^{-12}$	0.1	2650		
Damage zone	$k_x = 10^{-15}$ $k_z = 2 \times 10^{-15}$	0.05	2650	Corey (1954) $S_{lr} = 0.33$; $S_{gr} = 0.05$	van Genuchten $\lambda_{pcap} = 0.444$; $S_{lr} = 0.3$;

Hydrogeologic property	Permeability [m²]	Porosity	Rock grain density [kg/m³]	Relative permeability parameters	Capillary pressure parameters
					$1/P_0 = 1.485 \times 10^{-4}$[Pa^{-1}]; $P_{max} = 1.0 \times 10^8$[Pa]; $S_{ls} = 1.0$
Upper basaltic lavas Diatomites Miocene tuff		0.01	2650		
Rhyolitic lavas	$k_{x,z} = 10^{-16}$	0.1	2650		van Genuchten $\lambda_{pcap} = 0.444$; $S_{lr} = 0.4$; $1/P_0 = 1.485 \times 10^{-5}$[Pa^{-1}]; $P_{max} = 1.0 \times 10^8$[Pa]; $S_{ls} = 1.0$
Oligocene tuff		0.1	2450	Corey $S_{lr} = 0.43$; $S_{gr} = 0.05$	
Mezozoic metasediments		0.05	2550		
Older basaltic lavas Andesite-dacitic lavas	$k_{x,z} = 5 \times 10^{-16}$	0.01	2650		
Intrusive basement	$k_{x,z} = 10^{-19}$	0.01	2750		

a

λ_{relp}: van Genuchten λ for liquid relative permeability, S_{lr}: residual liquid saturation, S_{grmax}: maximum possible value of residual gas saturation, k_{rgmax}: maximum value of k_{rg}, γ: exponent in k_{rg}, λ_{gas}: van Genuchten λ for gas relative permeability.

b

λ_{pcap}: van Genuchten λ for capillary pressure, P_0: capillary strength parameter, P_{max}: maximum capillary pressure, S_{lmin}: saturation at which original van Genuchten capillary pressure goes to infinity.
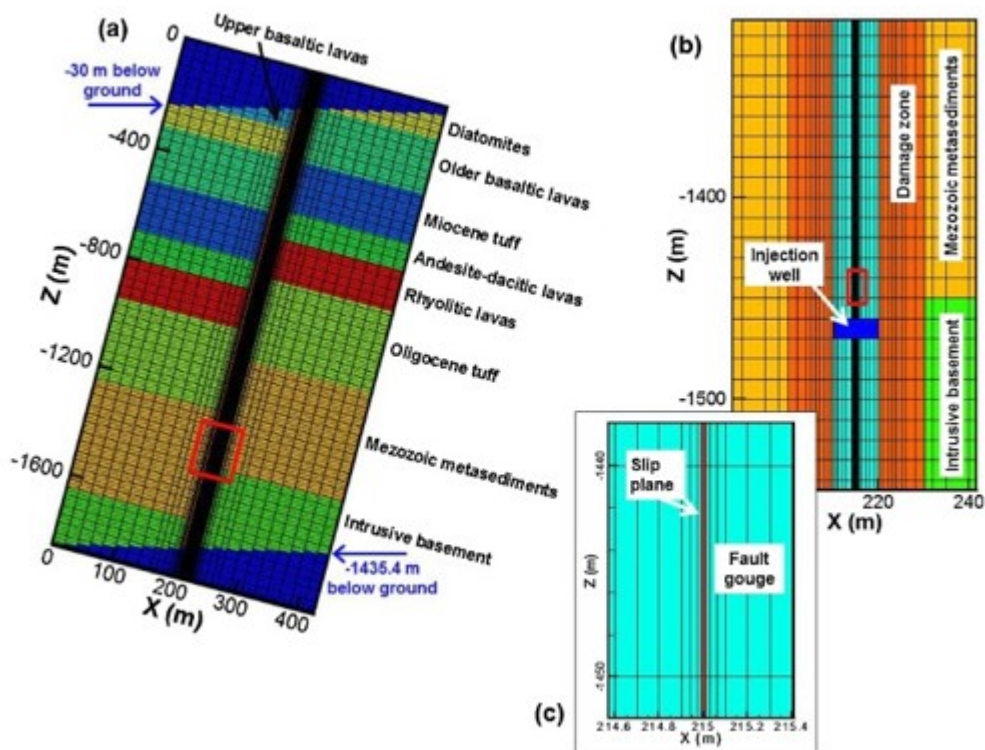
Fig. 2. 2D model grid: (a) the whole model domain (note that the dark blue triangular areas at the upper left and lower right corner are not part of the actual model domain); (b) the local area around the well; (c) a close-up of the area near the slip plane, showing the fine discretization.

The z-axis of the model is aligned along the dip of the fault, and the x-axis is in the direction across the fault. The grid is discretized uniformly in the z-direction ($dz = 10$ m), and more finely in the x-direction near the slip plane (from $dx = 20$ m at the far end of the matrix down to $dx = 2$ cm for the slip plane) as shown in Fig. 2. The width of the cells in the horizontal direction parallel to the fault direction (the y-direction) is 50 m. The grid is rotated clockwise by 30° to make the fault dip 60°. The model vertically extends from the water table, which is 30 m below the ground surface, to the depth of 1435.4 m below the surface. The injection/withdrawal well intersects the fault gouge at a depth of 1193 m. Note that the 10-m height of the grid block is used for the injection/withdrawal well without any further grid refinement. Thus, the model is not intended to accurately reproduce near-wellbore effects during CO_2 injection and withdrawal. The focus of the present study is on exploring whether we can gain additional information regarding EGS fault/ fractures from pressure transient data collected at offset monitoring wells during CO_2 push-pull testing.

In addition to the hydrological rock properties, Table 1 includes the parameters for multiphase flow. For the slip plane and fault gouge, the van Genuchten (1980) model is used to describe the liquid relative permeability and capillary pressure relations for the two-phase system of CO_2 and water. The maximum gas relative permeability (k_{rgmax}), which is defined as the relative permeability at the residual water saturation, is known to be typically smaller than unity (Levine et al., 2014). To take this into account in the fault gouge, where most of the injected CO_2 is expected to flow, for gas relative permeability we use the hysteretic form of the van Genuchten model (Lenhard and Parker, 1987) implemented in TOUGH2 (Doughty, 2013), which allows the user to define the maximum value of the gas relative permeability. In this study, k_{rgmax} is set as 0.5. For simplicity, hysteresis itself is turned off and the characteristic curves are the same for CO_2 drainage and imbibition. For the damage zone and matrix, where little CO_2 is expected to flow, we use the simpler Corey (1954)curves for two-phase relative permeability and the van Genuchten (1980)model for capillary pressure. Fig. 3 shows the characteristic curves of all rock types in the model.
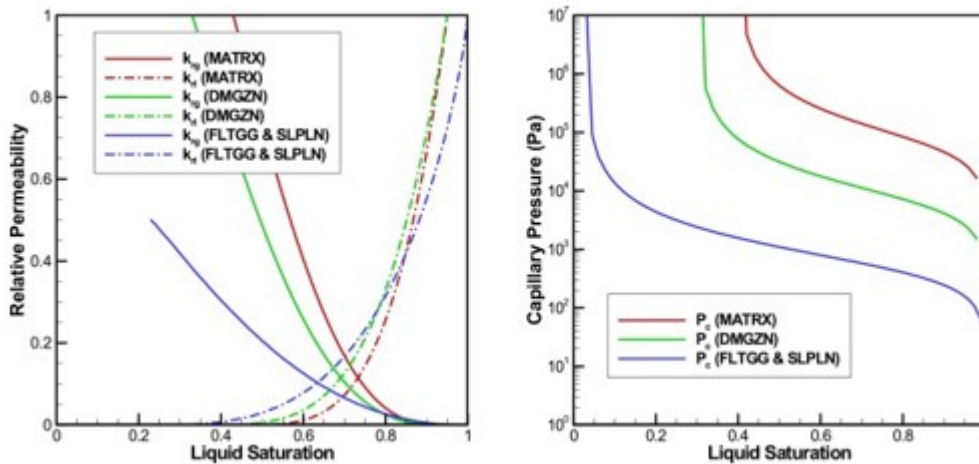

Fig. 3. Characteristic curves used for modeling slip plane (SLPLN), fault gouge (FLTGG), damage zone (DMGZN), and matrix (MATRX).

3.2. Initial and boundary conditions

The initial hydrostatic condition is based on the water table at 30 m below the ground surface. This initial hydrostatic condition is used to calculate the pressure difference $\Delta P = P - P_{init}$, which is the variable used in this study to describe all pressure-related data. Temperature varies from 25 °C at the top boundary to 170 °C at the depth of 630 m with a geothermal gradient of

0.24 °C/m, and to 210 °C at the bottom boundary with the geothermal gradient of 0.05 °C/m, which approximately represents field observations. The impact of salinity on pressure transient is not considered, and the salinity and the initial dissolved CO_2 concentration are assumed to be zero. The top and bottom boundaries are open to flow and the side boundaries are closed.

3.3. Push-pull and monitoring scenarios

The injection/withdrawal well is assumed to be open only in the fault gouge and slip plane, and a constant pressure of 0.3 MPa above and below the ambient hydrostatic pressure ($\Delta P_{inj} = 0.3$ MPa and $\Delta P_{wdraw} = -0.3$ MPa) is applied for injection and withdrawal of CO_2, respectively. CO_2 is injected for 4 days, then fluid comprising a mixture of CO_2 and brine is produced for 4 days from the same well. We assume the injected CO_2 is preheated to the ambient temperature of the geothermal reservoir. During the push period, the gas saturation at the injection well is set to be 0.99, and during the pull period, it is set to be zero. The injection/withdrawal rates of CO_2 and brine are calculated from the flux terms between the injection/withdrawal well and the adjacent fault zone grid blocks. We assume that additional observation wells are available for pressure monitoring and frequent well logging for the purpose of fault characterization, and several potential locations along the fault gouge are considered. Neutron capture cross section measured from well logging is sensitive to CO_2 saturation, and therefore can be used to estimate CO_2saturation in the fault gouge (Oldenburg et al., 2016). Here, we assume that CO_2 saturation data are available as the result of well logging analysis. Anticipating buoyancy effects on the CO_2 flow, the monitoring wells (MW) are located near the left-hand edge of the fault gouge (i.e., along the hanging wall) and are assumed to be located at 50 m, 100 m, and 200 m above the injection well along the z-direction (MW_{50m}, MW_{100m}, and MW_{200m}).

4. Forward simulation (base case) results

4.1. Variation of fluid flow rates during push and pull periods

Fig. 4 shows CO_2 and water flow from the injection well to the fault zone during the push and pull periods. Each curve in this plot represents the sum of the flows between the injection well and the adjacent fault zone grid

blocks. A negative value means the fluid flows from the fault zone into the well. As the injection starts, the overpressure in the injection well forces both CO_2 and water to flow out of the well. The CO_2 flow gradually decreases as the pressure difference between the injection well and the surrounding fault zone decreases. The flow rate drops at 10^3 s as a CO_2 phase develops in the grid block right above the injection well, and slightly declines again at 2×10^4 s as the pressure pulse reaches the top boundary of the model (a constant-head water table). Unlike CO_2, which mostly flows upward during the push period, water flows downward except at very early times (~30 s). On the other hand, during the pull period, the underpressure relative to the initial hydrostatic pressure pulls both CO_2 and water back into the well in proportions equal to the local mobility. However, CO_2 is no longer produced after about 1.3×10^3 s due to buoyancy effects which carry CO_2 upward and out of the capture zone of the producing well; altogether only 1.7% of the injected CO_2 is recovered. Water flow is reversed at late times, indicating the pressure above the withdrawal well is temporarily lower than that at the withdrawal well. This will be further discussed in the next section.
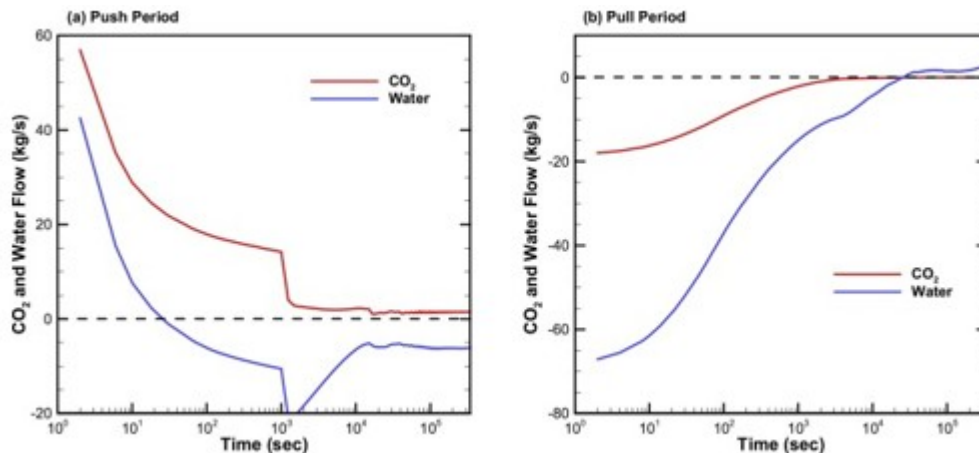

Fig. 4. CO_2 and water flow during the (a) push and (b) pull period.

4.2. Spatial distribution of pressure difference and gas saturation

Fig. 5 shows the spatial distribution of pressure difference (ΔP) and gas saturation during the push and pull periods. During the injection, the pressure pulse quickly propagates through the fault gouge and damage zone, taking only 2×10^4 s for the pressure pulse to reach the top model boundary through the fault gouge. The pressure also propagates relatively fast laterally through the andesite-dacitic lavas (see the distribution at the

end of the push period at ~700 m depth), where the permeability is five times greater than that in the other country rock formations. As the fluid withdrawal starts after 4 days of CO_2injection, underpressure relative to the initial hydrostatic pressure (i.e., negative ΔP) develops near the well, with the pressure decline most significant in the fault gouge during the pull period.
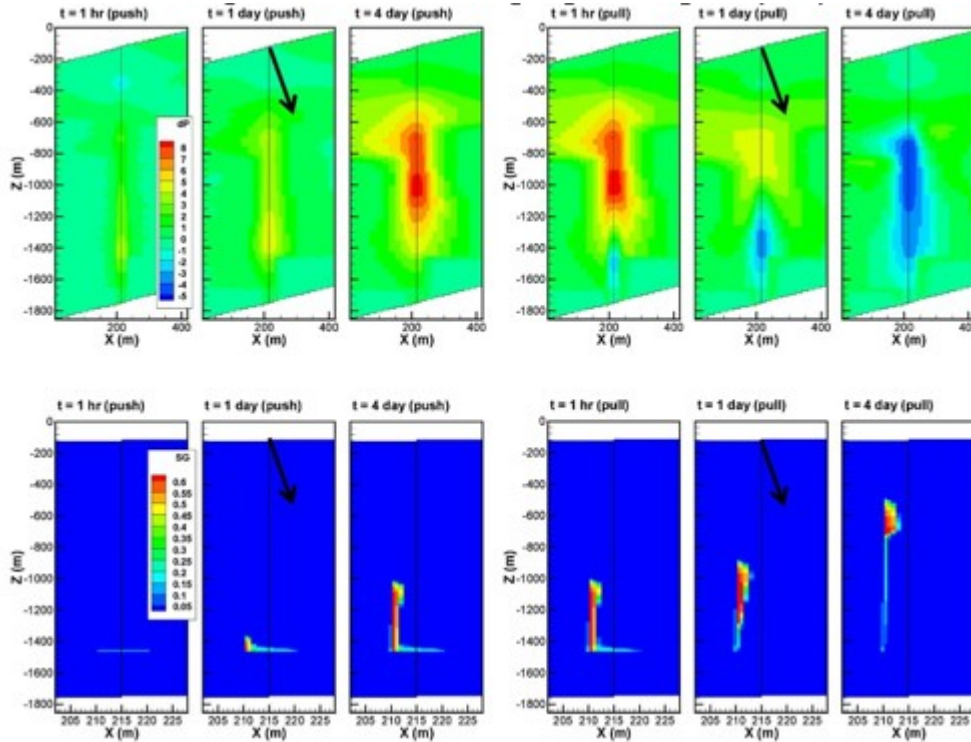

Fig. 5. Spatial distribution of pressure change in bar (upper row) and gas saturation (lower row) at 1 h, 1 day, and 4 days of the push and pull periods. Note that the actual grid is rotated clockwise by 30° to make the fault dip 60°; black arrows point in the vertical direction. Note that the range of the x-axis in gas saturation plots is much narrower than that in pressure change plots.

One thing that should be noted is that the maximum ΔP observed during the push period (~ 0.85 MPa) is higher than ΔP_{inj} (0.3 MPa), which is most evident at $t = 4$ day in Fig. 5. This is due to the effect of a gas column being created in the gouge. The pressure gradient in the gas column is much smaller than the pressure gradient in a water filled column, due to the much smaller density of gas compared to water. Thus, the pressure at the top of the gas plume is similar to the pressure at the base. This pressure forms the base of the water pressure profile above it in the gouge. As a result, the gouge water pressure becomes elevated. The maximum pressure decrease observed during the pull period is more than ΔP_{wdraw} as well. This is due to buoyancy

flow, which keeps pulling the CO_2 upward despite the underpressure at the well and consequently leaves a low pressure region in between the withdrawal well and the leading edge of the CO_2 plume.

During the push period, the injected CO_2 mainly flows upward through the fault gouge, specifically against the hanging wall due to the dipping angle of the fault and buoyancy of CO_2. This is because the transmissivity of the gouge is more than two orders of magnitude greater than that of the damage zone and matrix. Only a limited amount of CO_2 enters the damage zone because of its lower permeability and higher capillary pressure at the water-CO_2 interface. During the pull period, the CO_2 plume keeps moving upward, driven by a strong buoyancy force, despite the underpressure at the well. As a result, the leading edge of the CO_2 plume has traveled about 1000 m upward in the z-direction by the end of the simulation time (after four days of injection and four days of withdrawal). This explains the low CO_2 recovery rate during the pull period. Due to decompression and local pressure increase, the CO_2 plume tends to expand in the x-direction as CO_2 flows upward; it is most prominent at the end of the pull period.

4.3. Temporal change of pressure difference and gas saturation at selected monitoring locations

Fig. 6 shows the temporal variation of pressure transient and gas saturation at the selected monitoring wells. The pressure transient here and thereafter refers to the pressure difference (ΔP) as defined in Section 3.2. The pressure transients at the monitoring wells MW_{50m}, MW_{100m}, and MW_{200m} in general show a similar pattern during the push period. As the CO_2 injection starts, the pressure propagates from the injection well and a gradual pressure increase is observed. The pressure increases rather steeply when CO_2 reaches the monitoring location, due to decreasing total kinematic mobility, and drops when the CO_2 saturation reaches approximately 0.6, at which point the total kinematic mobility rises again according to the relative permeability functions shown in Fig. 3. Due to the distance from the injection well, the pressure transient increases in consecutive order from MW_{50m} to MW_{200m}. In addition, the injected CO_2 decompresses as it rises upward through the hydrostatic pressure of the resident water.
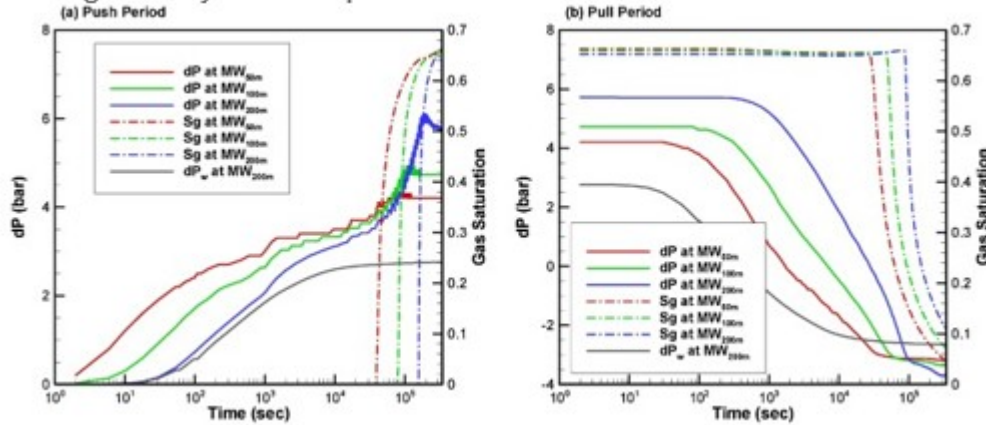
Fig. 6. Pressure transient (solid) and gas saturation (dash-dot) at MW_{50m}, MW_{100m}, and MW_{200m} during the push and pull periods. As a reference case, a pressure transient with water as an agent for the push-pull test (ΔP_w at MW_{200m}) is also shown.

The oscillations observed in the pressure transient during the push period are due to spatial discretization error. When CO_2 phase enters a grid block (e.g., CO_2 enters the grid block right above the injection well at ~10^3 sec), the grid block undergoes a transition from a single aqueous phase to a two-phase condition. The liquid relative permeability drops rapidly while the gas relative permeability increases rather slowly (see Fig. 3), resulting in a reduction of the total kinematic mobility of the fluid. As the gas saturation increases, the increase in gas relative permeability becomes greater than the decrease in liquid relative permeability. As a result, the total kinematic mobility varies in a parabolic manner as gas phase saturation increases. This pattern repeats every time CO_2 enters a new grid block, and pressure data show cyclic variations. The discretization error may not only cause such spurious pressure oscillations but also a systematic deviation from the true pressure transient, and can be minimized by using a finely gridded mesh (Pruess and García, 2002). This remedy may be conveniently applied for a radial flow problem because a high resolution mesh may only be needed near the injection well. But, it would require a significant increase in the number of cells for the linear flow geometry up the fault for the present problem. Since this study focuses on exploring the potential of pressure transient in fault/fracture characterization, not on calibrating or characterizing a real geothermal site, we view our rather coarse gridding in the z-direction, and the accompanying pressure oscillations, as acceptable. During the pull period, the pressure transients at MW_{50m}, MW_{100m}, and MW_{200m} decrease after a lag time, which proportionally increases with the

distance between the withdrawal well and the monitoring well. The lag time is associated with the pressure diffusion. CO_2 will keep flowing upward until the underpressure imposed at the withdrawal well propagates to the monitoring location. For the CO_2 push-pull, the lag time is additionally affected by the strong buoyant rise of CO_2. The gas saturation at the monitoring locations decreases because CO_2 keeps flowing upward and exits the fault zone, not because it is recovered at the withdrawal well.
Note that Fig. 6 includes as a comparison the pressure transient at MW_{200m} when water is used as an agent for the push-pull test (ΔP_w at MW_{200m}). The discussion regarding the effects of different injection fluids will be presented in Section 7.

5. Sensitivity analysis

We assess the sensitivity of pressure-transient and gas-saturation data to various model parameters and conditions. In order to compare the sensitivity of two different data types, we calculate scaled sensitivity coefficients, which normalize sensitivity coefficients by the a priori standard deviation of observation and the expected parameter variation. The standard deviations of pressure and gas saturation are 2×10^4 Pa and 0.05, respectively, and the initial guess and expected variation of the parameters are shown in Table 2. To calculate the total scaled sensitivity at each monitoring location, the scaled sensitivity coefficients at 30 discrete times are selected for each push and pull period, which is sufficient to capture the behavior of pressure transient in the log scale, and summed together.

Table 2. Initial guess and expected variation (in parentheses) of parameters used for sensitivity analysis.

Permeability parameters[a] [m^2]		Multiphase flow parameters	
Slip plane	−12.0 (0.2)	λ_{relp}	0.8 (0.1)
Fault gouge	−12.0 (0.2)	λ_{pcap}	0.444 (0.1)
Damage zone	−15.0 (0.2)	S_{lr}	0.23 (0.02)
Matrix	−16.0 (0.2)	P_0[a] [Pa]	2.699 (0.2)

a

The logarithms of permeability and capillary strength parameter (and their variation) are used for sensitivity analysis.

5.1. Permeability

Table 3 shows the total scaled sensitivity of pressure transient and gassaturation data to material permeability at MW_{50m}, MW_{100m}, and MW_{200m}. For both the push and pull periods, the pressure transient and gas saturation are most sensitive to the fault gouge permeability. The influence of the damage zone and matrix permeability on the pressure transient is minor, and on the gas saturation is even smaller since CO_2 mainly flows through the fault gouge. Among different monitoring locations, the sensitivity is the strongest at MW_{200m}. Thus, unless otherwise stated, we choose this location as our default monitoring well and show the results of this location for all the other analyses in this study.

Table 3. Total scaled sensitivity of pressure transient and gas saturation to permeability during push-pull testing. Fault gouge permeability is the most sensitive parameter, and observations at MW_{200m} (shown in bold) have the highest sensitivity.

		Slip plane permeability	Fault gouge permeability	Damage zone permeability	Matrix permeability	Total
Push period	ΔP at MW_{50m}	0.0	29.0	2.4	0.0	31.4
	ΔP at MW_{100m}	4.8	54.6	0.2	4.8	64.5
	ΔP at MW_{200m}	6.5	105.1	4.3	5.6	121.5
	S_g at MW_{50m}	0.0	24.8	1.2	1.3	27.3
	S_g at MW_{100m}	0.1	62.2	1.4	0.3	64.0
	S_g at MW_{200m}	0.6	110.4	0.2	0.2	111.5
Pull period	ΔP at MW_{50m}	0.0	23.2	0.2	0.7	24.2
	ΔP at MW_{100m}	1.4	40.6	2.9	2.2	47.1
	ΔP at MW_{200m}	0.2	**89.4**	2.9	1.2	93.7
	S_g at MW_{50m}	1.1	36.9	2.4	0.7	41.0
	S_g at MW_{100m}	0.9	52.6	0.6	1.0	55.1
	S_g at MW_{200m}	0.9	**68.1**	1.2	0.8	71.0

Even though Table 3 indicates that the total scaled sensitivities of pressure transient and gas saturation are similar, the temporal variations of scaled

sensitivity are quite different. Fig. 7 shows the scaled sensitivity of the pressure transient and gas saturation during the push period as a function of time. From early times of CO_2 injection, the pressure transient shows a significant sensitivity to fault gouge permeability (Fig. 7a). On the other hand, the sensitivity of gas saturation (Fig. 7b) is zero until the CO_2 plume reaches the monitoring location. Compared to the fast-propagating pressure pulse, the CO_2 plume migrates much more slowly, so no sensitivity is detected until late in the push period.
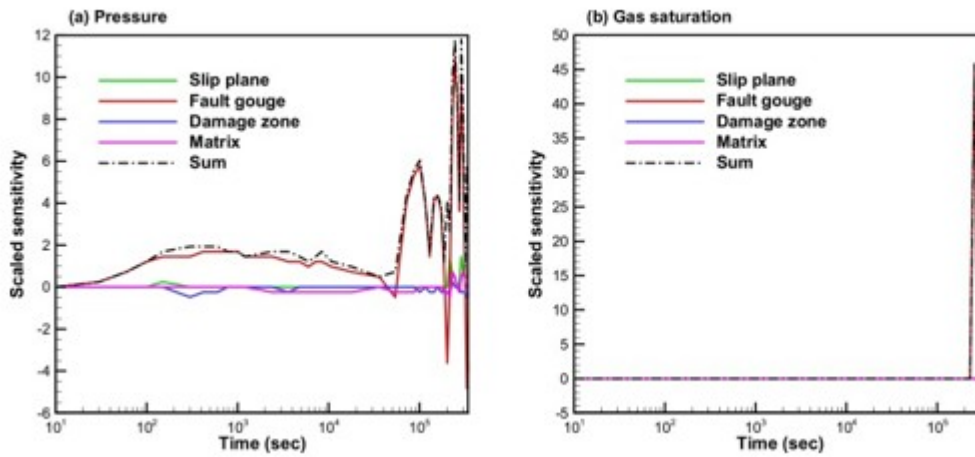

Fig. 7. Temporal variation of the scaled sensitivity to material permeabilities: (a) pressure transient and (b) gas saturation.

To exemplify the impact of material permeability on pressure transient, the pressure transients for different permeability conditions (varying the permeability of one material at a time) are plotted in Fig. 8. The fault gouge permeability varies over one order of magnitude, whereas the damage zone and matrix permeability differ over two orders of magnitude. However, the fault gouge permeability has the dominant impact on both the speed of the pressure propagation and the magnitude of the pressure buildup. When the damage zone or matrix permeability varies, the overall pressure transient is almost identical, consistent with the low sensitivity of the pressure transient to these permeabilities shown in Table 3. A noteworthy difference between Figs. 8b and 8c is that the impact of varying the damage zone or matrix permeability is observed at different times. When varying the damage zone permeability, the pressure transients differs mostly from 10 s to 10^3 s. On the other hand, when the matrix permeability is varied, the change in the pressure transient is observed between 10^3 sec and 10^5 sec. This difference

is due to the slow pressure propagation through these lower permeability materials. Because the damage zone is closer to the injection well, the impact of the damage zone permeability on the pressure transient is observed earlier than that of the matrix permeability.
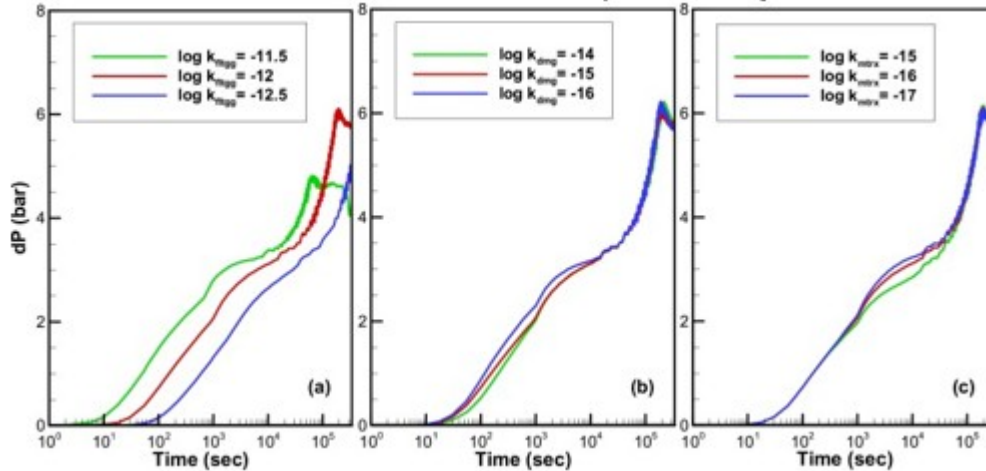

Fig. 8. Pressure transients for different permeability conditions: (a) fault gouge, (b) damage zone, and (c) matrix.

5.2. Multiphase flow parameters

To examine the effect of relative permeability and capillary functions on pressure transient and gas saturation data, we assessed the sensitivity to the multiphase flow parameters. Among the parameters used to describe the multiphase flow conditions, the most influential parameters are shown in Fig. 9, which are van Genuchten parameters for liquid relative permeability and capillary pressure, residual liquid saturation, and capillary strength parameter (λ_{relp}, λ_{pcap}, S_{lr}, and P_0). Because these parameters are related to multiphase flow, they start affecting the pressure transient after the CO_2 phase appears in the fault gouge. Unlike the material permeabilities, no parameter has a dominant influence on pressure transient and gas saturation. Their influence on the pressure and gas saturation is smaller than the fault gouge permeability, but more significant than the damage zone and matrix permeability.
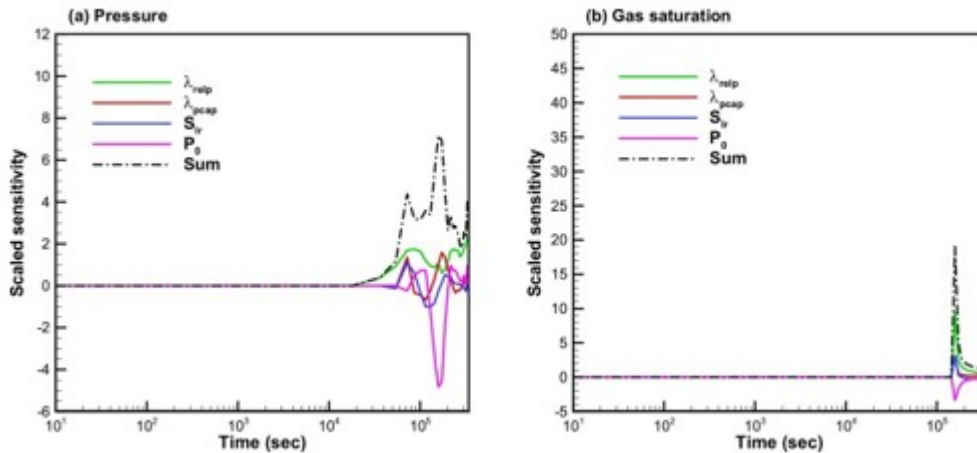
Fig. 9. Temporal variation of the scaled sensitivity to multiphase flow parameters: (a) pressure transient and (b) gas saturation.

The multiphase flow parameters are usually unknown at real EGS sites, and therefore it may be inevitable to have large uncertainties in these parameters. To examine the potential impact of the parameter uncertainty, we generated 50 sets of parameter combination using Latin Hypercube Sampling analysis (Zhang and Pinder, 2003) and simulate their impact on the pressure transient and gas saturation. The upper and lower limit of the range for each parameter is assigned to be 50% higher and lower, respectively, than the base value shown in Table 1. The results from the Monte Carlo simulations are visualized in Fig. 10. The thick black line shows the base case, and the other thin lines with different colors represent 50 Monte Carlo realizations. The Monte Carlo realizations of the pressure transient diverge soon after $\sim 10^3$ sec, when the CO_2 phase develops in the fault gouge, indicating that uncertainty in these multiphase flow parameters can significantly impair the accuracy of the fault characterization (i.e., calibrating the fault zone permeabilities). Fig. 10b also shows that both the arrival time of the CO_2 plume and the level of gas saturation in the CO_2 plume can greatly vary depending on the parameter combination.
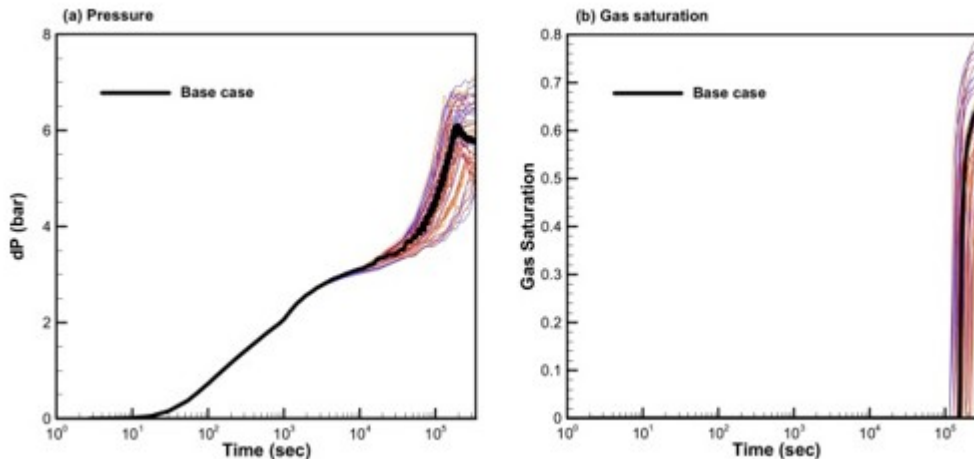
Fig. 10. Monte Carlo uncertainty propagation analysis: (a) pressure transient and (b) gas saturation. The thick black line shows the base case, and the other thin lines with different colors represent Monte Carlo realizations.

5.3. Boundary conditions (top and side)

We explored whether conditions at outer edges of the fault zone can be inferred from the pressure transient. In addition to the base case of an open-top fault, closed-top and semi-closed-top fault conditions are considered. The semi-closed top condition is represented by a caprock with the permeability of 10^{-16} m^2. As shown in Fig. 11, the pressure transient starts to differ when the pressure pulse reaches the fracture top at about 10^4 seconds. But, the most distinct difference among the cases is observed at late times. While the pressure transient in the base case declines and slowly stabilizes after the leading edge of the CO_2 plume passes the monitoring location, the pressure transients in the other two cases bounce back. The pressure buildup is more significant when the top boundary is completely closed than semi-closed. This result shows that the pressure transient analysis can be used to examine the connectivity of faults and fracture networks to overlying hydrologic systems or the surface.
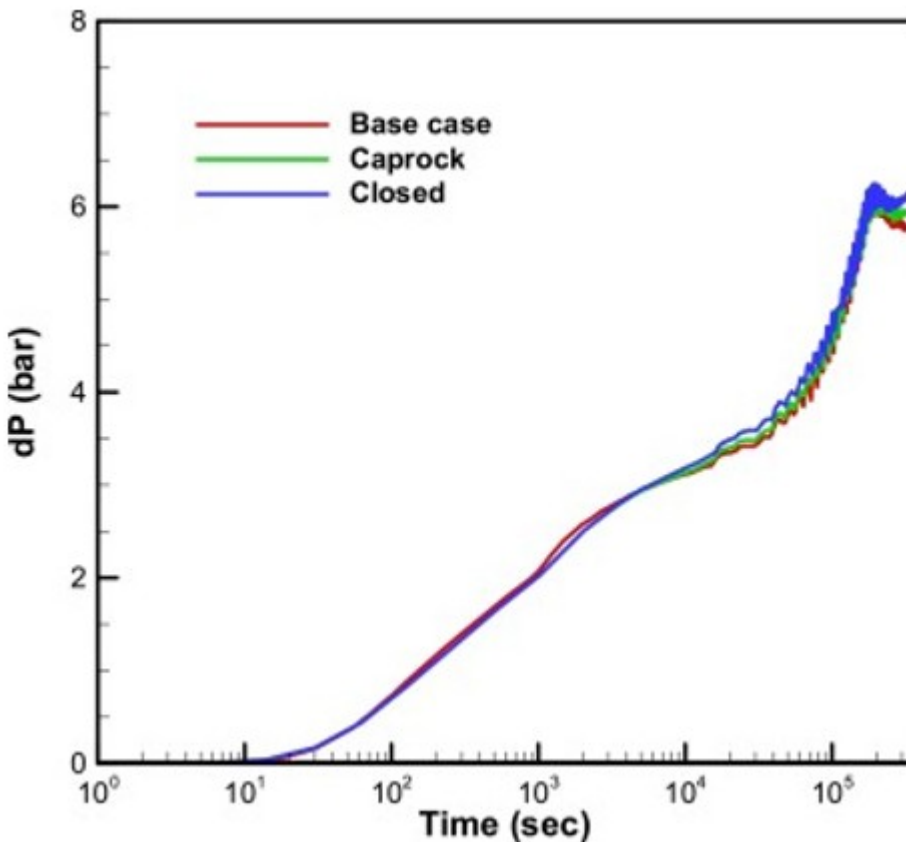
Fig. 11. Pressure transients for different top boundary conditions.

The effect of the side boundary condition is also evaluated. Compared to the base case of a closed side boundary, no difference in the pressure transient at any monitoring wells is observed for an open side boundary. Due to the low hydraulic diffusivity of the matrix, which is three orders of magnitude smaller than that of the fault gouge, the extent and magnitude of the pressure pulse transmitted through the matrix is much smaller than that through the fault gouge (see Fig. 5). As a result, the impact of the side boundary on the pressure transient is insignificant.

6. Fault characterization using the inverse modeling of synthetic data

Based on the sensitivity analysis result, we attempted fault characterization using synthetic data. The synthetic data for the push period are generated by running a forward simulation of the base case. The frequency of the data collection is denser at early times than at late times so that sufficient data points are available to capture the behavior of the pressure transient at early times on a log scale. Note that the leading edge of the CO_2 plume reaches the monitoring well locations at late times ($>3 \times 10^4$ sec, see Fig. 6) at which

point data are collected every 4 h. For this inverse modeling study, we suppose this logging frequency is feasible.

We assumed that the permeability of the fault gouge, damage zone, and matrix are unknown, and consider two different inversion scenarios: (1) pressure transients only are available for inversion, and (2) both pressure transient and gas saturation data are available. For each scenario, we explore the accuracy of the inversion depending on the location of the monitoring well and the number of parameters to be characterized; we examine all the potential monitoring well locations (MW$_{50m}$, MW$_{100m}$, and MW$_{200m}$) and estimate either only the fault gouge permeability or the permeabilities of the fault gouge, damage zone, and matrix. For all cases, the initial guess for each parameter is 10^{-13}, 10^{-14}, and 10^{-15} m², respectively. We present here the results obtained from these initial values, but other attempts with different combinations of initial guesses result in similar outcomes. Because the parameters are expected to vary over a large range of values, the logarithms of the parameters are estimated instead of the parameter values, and the inversion results reported in Table 4 are in log-space as well. All the other parameters are assumed to be known and error free for simplicity of the analysis.

Table 4. Estimated parameters for different inversion scenarios.

Number of estimated parameters		log k_{fltgg}		log k_{dmg}		log k_{mtrx}	
		True value -11.70		**True value** -14.70		**True value** -16.0	
		Initial guess −13.0		**Initial guess** −14.0		**Initial guess** −15.0	
		Estimate	Standard deviation	Estimate	Standard deviation	Estimate	Standard deviation
		Pressure transient alone					
1	MW$_{50m}$	−11.70	0.008				
	MW$_{100m}$	−11.67	0.011				
	MW$_{200m}$	−11.67	0.011				
3	MW$_{50m}$	−12.50	0.041	−14.04	0.262	−15.06	1.5e + 50
	MW$_{100m}$	−12.25	0.015	−11.77	0.022	−17.59	0.081
	MW$_{200m}$	−12.20	0.019	−11.70	0.020	−14.88	0.109
		Pressure transient plus gas saturation data					
1	MW$_{50m}$	−11.85	0.010				
	MW$_{100m}$	−11.79	0.006				

	log k_{fltgg}		log k_{dmg}		log k_{mtrx}	
True value	**-11.70**		**-14.70**		**-16.0**	
Initial guess	−13.0		−14.0		−15.0	
Number of estimated parameters	Estim ate	Standard deviation	Estim ate	Standard deviation	Estim ate	Standard deviation
MW$_{200m}$	−11.77	0.001				
3 MW$_{50m}$	−11.82	0.008	−14.18	0.129	−21.37	N/A
MW$_{100m}$	−11.75	0.005	−13.08	0.051	−29.52	N/A
MW$_{200m}$	−12.16	2.268	−11.71	2.995	−14.97	7.702

6.1. Pressure transient alone

When only the fault gouge permeability is estimated, the estimate is quite accurate for all monitoring locations as shown in Table 4. The inaccurate values for the other permeabilities (the initial guesses shown in Table 4) have no effect on the inversion. This is explained by the low sensitivity of the pressure transient to the permeability of the damage zone and matrix (see Table 3). On the other hand, when all the permeabilities are estimated, the accuracy of the estimates is poor. Particularly, at MW$_{100m}$, and MW$_{200m}$, the damage zone permeability is estimated higher than the fault gouge permeability, indicating this inversion problem is non-unique and alternative information would be required to constrain the model. The uncertainty of the estimated matrix permeability at MW$_{50m}$ is huge due to the insensitivity of pressure transient to the matrix permeability.

6.2. Pressure transient plus saturation data

When only the fault gouge permeability is estimated using the pressure transient and saturation data, the estimated permeabilities are close to the true value of $2.0 \times 10^{-12}\,\text{m}^2$ (from $1.4 \times 10^{-12}\,\text{m}^2$ at MW$_{50m}$ to $1.7 \times 10^{-12}\,\text{m}^2$ at MW$_{200m}$), but slightly worse than those estimated with pressure transient alone (from $2.0 \times 10^{-12}\,\text{m}^2$ at MW$_{50m}$ to $2.2 \times 10^{-12}\,\text{m}^2$ at MW$_{200m}$). When all the permeabilities are estimated, the inversion accuracy for the fault gouge permeability at MW$_{50m}$ and MW$_{100m}$ is improved compared to the previous scenario of pressure transient only (see Table 4). But, the estimate at MW$_{200m}$($7.0 \times 10^{-13}\,\text{m}^2$) is still relatively poor. This is due to the distance between MW$_{200m}$ and the injection well. The gas saturation data are available only for much later times ($>2 \times 10^5$ s) at MW$_{200m}$. However, with the initial

guess of 10^{-13} m^2 for the fault gouge permeability, the CO_2 plume migrates much too slowly and no increase in gas saturation at MW$_{200m}$ is simulated. As a result, the gas saturation observation data have no contribution to the calibration of the parameters during the whole inversion, and the estimates are similar to those calibrated with only pressure transient data.

While the addition of gas saturation data helps constrain the model, the effect is mostly limited to the fault gouge permeability, which is expected since the CO_2 plume mainly flows through the fault gouge. The accuracy of the inversion for the other parameters is actually worse, particularly for the matrix permeability at MW$_{50m}$, and MW$_{100m}$. Due to the insensitivity to this parameter, the difference between two successive iterations is too large, and the standard deviation of the estimate for the matrix permeability cannot be calculated, which leads to the termination of the inversion.

Overall, the added benefit from gas saturation data is surprisingly minor. The reason for this is apparent from the temporally limited contribution of gas saturation data. As shown in Table 3 and Fig. 7 for the base case, while the total sensitivity of pressure transient and gas saturation is similar to each other, the sensitivity of gas saturation is only observed at late times. To be more specific, the gas saturation is sensitive to the parameter only when the gas saturation varies. The sensitivity is zero until the CO_2 plume reaches the monitoring well, and the sensitivity quickly drops once the gas saturation begins to plateau.

7. CO_2 vs water as an agent for push-pull testing

This section discusses the effect of using CO_2 as an agent for push-pull analysis instead of water. Fig. 6 shows the pressure transient at MW$_{200m}$ when water is used as an agent for the push-pull test, along with pressure transients from CO_2 push-pull test. When water is injected, the pressure transient smoothly increases until it reaches ΔP_{inj}. Similarly, when water is produced, the pressure transient is reduced down to ΔP_{wdraw}. The whole system is a single-phase throughout the push-pull test (i.e., no multiphase flow effect and no buoyancy effect). Furthermore, compared to the CO_2/water mixture, which has smaller transmissivity due to relative permeability effects and smaller diffusivitydue to larger compressibility, the pressure signal is transmitted quickly through the fault gouge.

To examine the effect of the agent for push-pull analysis on fault characterization, we attempt to calibrate the fault gouge permeability using ΔP_w at MW_{200m} as described in Section 6 for CO_2 push-pull test. The estimated fault gouge permeability is $3.3 \times 10^{-12}\,m^2$, which is close enough to the true value of $2.0 \times 10^{-12}\,m^2$ but worse than the estimated value using the pressure transient during CO_2 push-pull test ($2.2 \times 10^{-12}\,m^2$). Such difference in accuracy may be augmented if data noise or model uncertainties are considered. When data are noisy, the notable pressure transient features observed during the CO_2 push-pull, such as the bumps and drops of the pressure transient dependent on CO_2 saturation, may help improving the inversion accuracy compared to the rather simple pressure transient during the water push-pull. On the other hand, the uncertainty in the multiphase flow parameters may make the calibration a highly ill-posed inverse problem. We try to invert the fault gouge permeability and two multiphase flow parameters (λ_{relp} and P_0) using pressure transients only and both pressure transient and gas saturation data. In general, the fault gouge permeability is most accurately estimated, and P_0 is least accurately estimated. The addition of gas saturation data has little impact on improving the accuracy of the inversion, but instead worsens the overall accuracy of the estimated parameters.

8. Concluding remarks

To investigate the feasibility of using pressure transient during CO_2 push-pull tests for EGS characterization, we have developed a 2D model with a single fault zone and simulated pressure transient data during the CO_2 push-pull test into the fault. The injected CO_2 mostly flows upward through the fault gouge, a core of the fault zone, because the fault gouge has the biggest transmissivity by over two orders of magnitude. As a result, the pressure transient mainly reflects the gouge properties, such as permeability and outer edge condition. Our study shows that the pressure transient is most sensitive to the fault gouge permeability. Consequently, the fault gouge permeability is most accurately estimated using the pressure transient data for inverse modeling. We also found that the local change in pressure at monitoring locations far above the injection point can be larger than the injection-induced pressure change at the injection well. This phenomenon occurs because of the gas column formed by the CO_2 and its

lower density relative to brine. In short, the top of the gas column exerts its pressure on the water column in the fault zone above, and the associated overpressure exerted can be much larger than the injection overpressure itself.

Another interesting finding is that the pressure transient is strongly influenced by multiphase flow conditions, which arise when injected CO_2 forms a phase separate from water in the fault. The pressure transient is more complicated than the case with water as an agent for push-pull testing because both transmissivity and pressure diffusivity are sensitive to relative permeabilities, which in turn are sensitive to both gas saturation and the parameters of the relative permeability functions (Table 1). Therefore, we suggest that site characterization should be done during a first water push-pull experimental phase. While such sensitivity to multiphase flow effects is desirable for improving the accuracy of site characterization, at this time the typical lack of knowledge of multiphase flow model parameters effectively limits the accuracy of the parameters characterization.

References

Borgia et al., 2015
A. Borgia, C.M. Oldenburg, R. Zhang, L. Pan, S. Finsterle, T.S.Ramakrishnan**Simulations of CO₂ push-pull in fractures to enhance geophysical contrast for characterizing EGS sites**
Proceedings, TOUGH Symposium 2015, Lawrence Berkeley National Laboratory, Berkeley, California (2015)
Borgia et al., 2017a
A. Borgia, C.M. Oldenburg, R. Zhang, Y. Jung, K.J. Lee, C. Doughty, T.M.Daley, B. Altundas, N. Chugunov, T.S. Ramakrishnan**Simulations of carbon**

dioxide injection, seismic monitoring, and well logging for enhanced characterization of faults in geothermal systems
Proceedings, 42nd Workshop on Geothermal Reservoir Engineering, Stanford University, Stanford, California (2017)

Borgia et al., 2017b
A. Borgia, C.M. Oldenburg, R. Zhang, L. Pan, T.M. Daley, S. Finsterle, T.S.Ramakrishnan**Simulating CO_2 injection into fractures and faults for Improved characterization of EGS sites**
Geothermics (2017), pp. 189-201, 10.1016/j.geothermics.2017.05.002

Corey, 1954
A.T. Corey**The interrelation between gas and oil relative permeabilities**
Producers Mon. (1954), pp. 38-41
(November)

Doughty, 2013
C. Doughty**User's Guide for Hysteresis Capillary Pressure and Relative Permeability Functions in TOUGH2, Report LBNL-6533E**
Lawrence Berkeley National Laboratory, Berkeley, Calif (2013)

Faulds et al., 2004
J.E. Faulds, M. Coolbaugh, G. Blewitt, C.D. Henry**Why is Nevada in hot water? Structural controls and tectonic model of geothermal systems in the northwestern Great Basin**
Geotherm. Resour. Counc. Trans., 28 (2004), pp. 649-654

Faulds et al., 2010
J.E. Faulds, M.F. Coolbaugh, D. Benoit, G. Oppliger, M. Perkins, I. Moeck, P.Drakos**Structural controls of geothermal acitivty in the Northern Hot Springs Mountains, Western Nevada: The tale of three geothermal systems (Brady's, desert peak, and desert queen)**
Geotherm. Resour. Counc. Trans., 34 (2010), pp. 675-683

Faulds et al., 2012
J.E. Faulds, A.R. Ramelli, L.J. Garside, M.F. Coolbaugh, H.L. Green**Preliminary geologic map of the Desert Peak quadrangle**
Nevada Bureau of Mines and Geology OF 12–5, Churchill County, Nevada (2012)
(scale 1:24,000)

Finsterle and Zhang, 2011
S. Finsterle, Y. Zhang**Solving iTOUGH2 simulation and optimization problems using the PEST protocol**

Environ. Modell. Softw., 26 (7) (2011), pp. 959-968, 10.1016/j.envsoft.2011.02.008

Finsterle et al., 2016

S. Finsterle, M. Commer, J. Edmiston, Y. Jung, M.B. Kowalsky, G.S.H.Pau, H. Wainwright, Y. Zhang**iTOUGH2: a simulation-optimization framework for analyzing multiphysics subsurface systems**

Comput. Geosci. (2016), 10.1016/j.cageo.2016.09.005

Finsterle, 1993

S. Finsterle**ITOUGH2 Users Guide Version 2.2 (No. LBL–34581)**

Lawrence Berkeley Lab., CA (United States) (1993)

Finsterle, 2004

S. Finsterle**Multiphase inverse modeling: review and iTOUGH2 applications**

Vadose Zone J., 3 (2004), pp. 747-762

Gudmundsson et al., 2002

A. Gudmundsson, I. Fjeldskaar, S.L. Brenner**Propagation pathways and fluid transport of hydrofractures in jointed and layered rocks in geothermal fields**

J. Volcanol. Geotherm. Res., 116 (3) (2002), pp. 257-278

Lenhard and Parker, 1987

R.J. Lenhard, J.C. Parker**A model for hysteretic constitutive relations governing multiphase flow, 2. Permeability-saturation relations**

Water Resour. Res., 23 (12) (1987), pp. 2197-2205

Levine et al., 2014

J.S. Levine, D.S. Goldberg, K.S. Lackner, J.M. Matter, M.G. Supp, T.S.Ramakrishnan**Relative permeability experiments of carbon dioxide displacing brine and their implications for carbon sequestration**

Environ. Sci. Technol., 48 (2014), pp. 811-818

Oldenburg et al., 2016

C.M. Oldenburg, T.M. Daley, B. Andrea, R. Zhang, C. Doughty, T.S.Ramakrishnan, B. Altundas, N. Chungunov**Preliminary simulations of carbon dioxide injection and geophysical monitoring to improve imaging and characterization of faults and fractures at EGS Sites**

Proceedings, 41 st Workshop on Geothermal Reservoir Engineering, Stanford University, Stanford, California (2016)

Pan et al., 2016

L. Pan, N. Spycher, C. Doughty, K. Pruess**ECO2N V2.0: A TOUGH2 fluid property module for modeling CO2-H2O-NaCL systems to elevated temperatures of up to 300 °C**

Greenhouse Gases Sci. Technol. (2016), 10.1002/ghg.1617

Pruess and García, 2002

K. Pruess, J. García**Multiphase flow dynamics during CO2 disposal into saline aquifers**

Environ. Geol., 42 (2002), pp. 282-295, 10.1007/s00254-001-0498-3

Pruess et al., 2012

K. Pruess, C. Oldenburg, G. Moridis**TOUGH2 User's Guide, Version 2.1, Report LBNL-43134**

Lawrence Berkeley Laboratory, Berkeley, Calif (2012)

Shevenell and De Rocher, 2005

L. Shevenell, T. De Rocher**Evaluation of chemical geothermometers for calculating reservoir temperatures at Nevada geothermal power plants**

Geotherm. Resour. Counc. Trans., 29 (2005), pp. 303-308

van Genuchten, 1980

M.T. van Genuchten**A closed-form equation for predicting the hydraulic conductivity of unsaturated soils**

Soil Sci. Soc. Am. J., 44 (5) (1980), pp. 892-898

Zhang and Pinder, 2003

Y. Zhang, G. Pinder**Latin hypercube lattice sample selection strategy for correlated random hydraulic conductivity fields**

Water Resour. Res., 39 (8) (2003), p. 1226, 10.1029/2002WR001822

Zhang et al., 2015

R. Zhang, D. Vasco, T.M. Daley, W. Harbert**Characterization of a fracture zone using seismic attributes at the In Salah CO$_2$storage project**

Interpretation, 3 (2) (2015), pp. SM37-SM46